AGU PUBLICATIONS

JGR

Journal of Geophysical Research: Oceans

RESEARCH ARTICLE

10.1002/2016JC012162

Sea surface pCO_2 and O_2 dynamics in the partially ice-covered Arctic Ocean

Fakhrul Islam[1], Michael D. DeGrandpre[1], Cory M. Beatty[1], Mary-Louise Timmermans[2], Richard A. Krishfield[3], John M. Toole[3], and Samuel R. Laney[4]

[1]Department of Chemistry and Biochemistry, University of Montana, Missoula, Montana, USA, [2]Department of Geology and Geophysics, Yale University, New Haven, Connecticut, USA, [3]Department of Physical Oceanography, Woods Hole Oceanographic Institution, Woods Hole, Massachusetts, USA, [4]Biology Department, Woods Hole Oceanographic Institution, Woods Hole, Massachusetts, USA

Key Points:
- Arctic Ocean sea surface pCO_2 and dissolved O_2 dynamics are examined using in situ sensors
- Variability in low ice regions was dominated by air-sea gas exchange, net community production, and advection/mixing
- Variability in high ice regions was dominated by horizontal advection with negligible contribution from net community production

Correspondence to:
M. DeGrandpre,
michael.degrandpre@umontana.edu

Citation:
Islam, F., M. D. DeGrandpre, C. M. Beatty, M.-L. Timmermans, R. A. Krishfield, J. M. Toole, and S. R. Laney (2017), Sea surface pCO_2 and O_2 dynamics in the partially ice-covered Arctic Ocean, *J. Geophys. Res. Oceans*, *122*, doi:10.1002/2016JC012162.

Received 19 JUL 2016
Accepted 9 DEC 2016
Accepted article online 22 DEC 2016

Abstract Understanding the physical and biogeochemical processes that control CO_2 and dissolved oxygen (DO) dynamics in the Arctic Ocean (AO) is crucial for predicting future air-sea CO_2 fluxes and ocean acidification. Past studies have primarily been conducted on the AO continental shelves during low-ice periods and we lack information on gas dynamics in the deep AO basins where ice typically inhibits contact with the atmosphere. To study these gas dynamics, in situ time-series data have been collected in the Canada Basin during late summer to autumn of 2012. Partial pressure of CO_2 (pCO_2), DO concentration, temperature, salinity, and chlorophyll-a fluorescence (Chl-*a*) were measured in the upper ocean in a range of sea ice states by two drifting instrument systems. Although the two systems were on average only 222 km apart, they experienced considerably different ice cover and external forcings during the 40–50 day periods when data were collected. The pCO_2 levels at both locations were well below atmospheric saturation whereas DO was almost always slightly supersaturated. Modeling results suggest that air-sea gas exchange, net community production (NCP), and horizontal gradients were the main sources of pCO_2 and DO variability in the sparsely ice-covered AO. In areas more densely covered by sea ice, horizontal gradients were the dominant source of variability, with no significant NCP in the surface mixed layer. If the AO reaches equilibrium with atmospheric CO_2 as ice cover continues to decrease, aragonite saturation will drop from a present mean of 1.00 ± 0.02 to 0.86 ± 0.01.

1. Introduction

The Arctic Ocean (AO) is changing rapidly. Decreasing sea ice thickness and extent [*Perovich et al.*, 2003, 2007; *Maslanik et al.*, 2007; *Krishfield et al.*, 2014], freshening of the sea surface [*Yamamoto-Kawai et al.*, 2009a], changing mixed layer dynamics [*Toole et al.*, 2010], and changes in the magnitude and timing of primary production [*Søreide et al.*, 2010; *Arrigo and van Dijken*, 2015] indicate that the AO is no longer in steady state. It is possible that decreasing sea ice extent has increased air-sea exchange of CO_2 leading to higher surface ocean CO_2 levels [*Cai et al.*, 2010] and accelerating ocean acidification [*Steinacher et al.*, 2009]. However, it remains uncertain whether the deep AO basins will uptake significant atmospheric CO_2 under seasonal ice-free conditions. Rapid equilibration and warming of the shallow isolated surface water and weak biological CO_2 drawdown are hypothesized to limit CO_2 invasion, keeping the ice-free central AO basins from becoming large atmospheric CO_2 sinks [*Cai et al.*, 2010].

Sea surface pCO_2 data sets from the central AO basins are scarce, with most prior studies focusing on nearshore and shelf areas [*Anderson et al.*, 2009; *Bates et al.*, 2006; *Kaltin and Anderson*, 2005; *Murata and Takizawa*, 2003]. Shipboard measurements made in the AO basins have generally found pCO_2 levels significantly below atmospheric saturation [*Anderson and Kaltin*, 2001; *Jutterström and Anderson*, 2010; *Bates*, 2006; *Bates et al.*, 2006; *Cai et al.*, 2010; *Else et al.*, 2013; *Robbins et al.*, 2013; *Evans et al.*, 2015]. However, almost all the studies cited above were based on ship data collected during low-ice conditions in summertime, which do not address the significant gaps that continue to exist in our understanding of sea surface CO_2 evolution in the AO, especially under ice. Moreover, few studies have specifically focused on short-term under ice CO_2 dynamics yet the sum of these processes drive seasonal and interannual variability. To examine pCO_2 variability on longer time scales in the central AO basins, we deployed pCO_2, dissolved oxygen

(DO), temperature (T), salinity (S), and bio-optical sensors on Ice-Tethered Profilers (ITPs) in the Canada Basin in late August 2012. Two ITPs were deployed in densely and sparsely ice-covered locations, providing a unique opportunity to compare CO_2 and DO variability under differing ice cover conditions. In 2012, the AO had the lowest seasonal ice extent since the beginning of the satellite record [*Parkinson and Comiso*, 2013; *Zhang et al*., 2013]. A strong storm that swept over the central AO in early August rapidly enhanced ice melt and decreased ice thickness [*Parkinson and Comiso*, 2013]. Our sensors were deployed a few weeks after the storm and ~2 weeks before the ice extent reached its minimum on 16 September 2012. The goal of this paper is to evaluate and compare the gas dynamics for these two biogeochemical data sets, to establish the extent to which ice cover alters the spatial and temporal variability of these gases in the upper ocean. The gas exchange fluxes have been quantified and discussed in a previous manuscript [*Islam et al*., 2016].

2. Methods

2.1. Study Site

The Canada Basin is the largest subbasin of the Arctic Ocean with an average depth of 3800 m (Figure 1). The basin has low surface salinity (average ~28) with a strong subsurface halocline located between 12 and 40 m [e.g., *Toole et al*., 2010]. This halocline is a complex mixture of water from the Eurasian Basin and Pacific Ocean [*Itoh et al*., 2007]. Horizontal variations in density, temperature, and salinity are common on ~1 km scale beneath sea ice cover [*Timmermans et al*., 2012]. The loss of both multiyear and first-year ice has been greater in the Canada Basin than any other AO basin [*McLaughlin et al*., 2011]. This region has been the focus of repeated hydrographic cruises since 2003 as part of the U.S. Beaufort Gyre Exploration Project and Beaufort Gyre Observing System (BGOS) which include mooring and ITP deployments [*Toole et al*., 2011; *Krishfield et al*., 2008].

We deployed a suite of instruments at ~6 m depth on two ITPs, ITP-64 and ITP-65, in the southern Canada Basin. ITP-65 was deployed on a 1.5 m thick ice floe on 27 August 2012 at 80° 53′ N, 137° 26′ W, and ITP-64 was deployed in open water because of limited ice extent on 28 August 2012 at 78° 47′ N, 136° 40′ W. The two systems were initially located 245 km apart from each other (Figure 1). ITP-64 and ITP-65 drifted 513 and 575 km, respectively, during the 40–50 day period when the sensors transmitted data (Figure 1).

2.2. In Situ Sensors

ITPs consist of a surface buoy that houses an inductive modem, GPS receiver and Iridium satellite phone, a jacketed, wire rope that extends to the end of the profiling range (600–800 m), and an instrumented profiler (McLane Research Laboratories, Inc.) containing a conductivity-temperature-depth sensor (CTD) (SBE41CP, Sea-Bird Electronics Inc.), DO sensor (SBE43I, Sea-Bird Electronics Inc.), and a custom bio-optical package [*Krishfield et al*., 2008; *Laney et al*., 2014]. The bio-optical package included a photosynthetically active radiation (PAR) sensor (PAR-LOG, Satlantic Inc.) and a "triplet" fluorometer (ECO FLbb-CD, WET Labs Inc.) that measured chlorophyll (Chl-*a*) fluorescence, colored dissolved organic matter fluorescence and optical

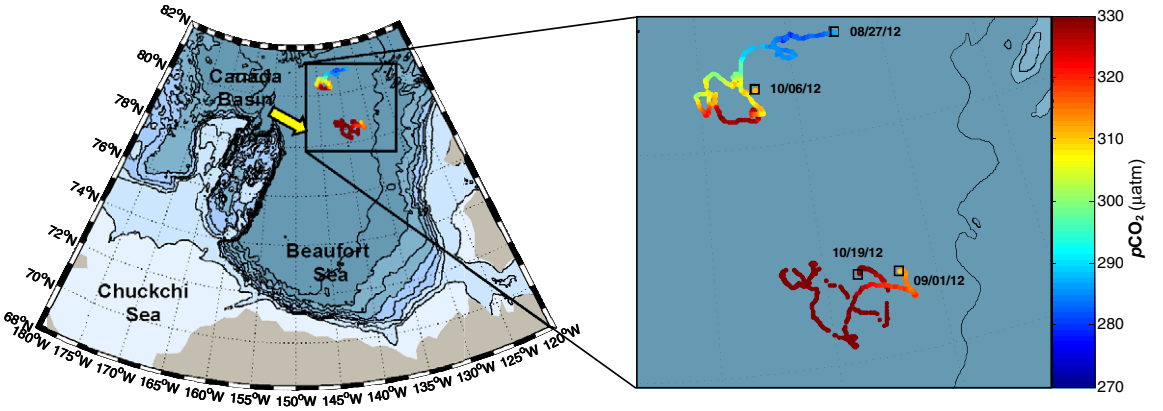

Figure 1. The study area (inset) is shown with the ITP-64 and ITP-65 drift tracks overlaid. Measurement start and end locations are highlighted by rectangular boxes labeled with dates. The pCO_2 values are shown in color. The track above 80°N corresponds to ITP-65.

backscatter. The ITP surface buoy is designed to make open water deployments possible. The ITPs profiled from ~7 to 760 m depth with six one-way profiles (two deep to 760 m, and four shallow to 200 m) every 1.5 days in summer (March–October) and four one-way profiles (two deep and two shallow) every 3 days in winter (November–February). All data collected by the ITPs were transmitted to the surface with inductive modems and were telemetered via Iridium satellite. The transmitted data were downloaded, processed, and made available at the Woods Hole Oceanographic Institution (WHOI) website (http://www.whoi.edu/itp). All bio-optical sensors were calibrated separately as described by *Laney et al*. [2014]. Calibration details of other sensors on the profilers are summarized in *Krishfield et al*. [2008].

Submersible Autonomous Moored Instruments for CO_2 (SAMI-CO_2, Sunburst Sensors, LLC) were interfaced with the ITP surface buoy to obtain time series measurements of the partial pressure of CO_2 (pCO_2) at 2 h intervals. The instruments also logged data from attached DO sensors (Optode 4175, Aanderaa Data Instruments) and CTDs (SBE37SI, Sea Bird Electronics Inc.). The DO sensors provided higher temporal resolution data in the surface ocean than possible with the DO sensor on the profiling vehicle. The pCO_2, DO, and CTD sensors were distributed at ~6 m with depths differing by <0.5 m. SAMIs passed all data to the ITP surface buoy through an inductive modem interface (SBE UIMM, Sea-Bird Electronics Inc.). Before deployment, each SAMI was calibrated at ~1°C over the expected pCO_2 range [*DeGrandpre et al*., 1995]. The calibration was corrected to the in situ temperature measured by the SAMI using the measurement temperature coefficient. The SAMI-CO_2 instruments have been shown to have minimal drift and do not require in situ calibration [*DeGrandpre et al*., 1995; *Gray et al*., 2011]. The DO sensors were calibrated in the lab using both an air-saturated solution and a zero DO solution at room temperature. All instruments were connected to the ITP platform and tested off the WHOI dock prior to deployment. Data were quality controlled using shipboard samples and data collected at the time of deployment (see below).

2.3. Other Supporting Data

Other data used in these analyses were obtained from different platforms or Internet sources. The hydrographic data collected during the cruise are available from the Beaufort Gyre Exploration Program based at the Woods Hole Oceanographic Institution (http://www.whoi.edu/beaufortgyre) in collaboration with researchers from Fisheries and Oceans Canada at the Institute of Ocean Sciences. The wind speed data near the ITP locations were downloaded from the European Centre for Medium-Range Weather Forecasts (http://apps.ecmwf.int/datasets/data/interim-full-daily). Barometric pressure and air temperature data were obtained from an Ice-Mass Balance (IMB) Buoy deployed on the same ice flow as ITP-65 (http://imb.erdc.dren.mil/2012L.htm). Hourly average mole fractions of atmospheric CO_2 (xCO_2) measured at Barrow, Alaska were obtained from the NOAA Earth System Research Laboratory (http://www.esrl.noaa.gov/gmd/dv/data). Ice coverage data were obtained from the National Snow and Ice Data Center (NSIDC) (http://nsidc.org/data). We computed PAR rather than use the profiler PAR data. Irradiance data from radiometers placed under heterogeneous sea ice cover do not necessarily provide a representative view of the under ice light field [*Frey et al*., 2011] and infrequent visits to the surface limited the usefulness of the PAR data. Therefore, to generate proxy time series of under ice PAR for modeling purposes, we used the surface solar radiation that corresponded to the ITP locations throughout their drift tracks. These values were scaled using the surface irradiance data collected on the ship to account for the nearly constant cloud cover. The attenuation expected through ice was estimated using data presented in *Long et al*. [2015].

Water density was calculated using in situ temperature and salinity at corresponding depths. The freezing point of seawater for a given depth was calculated using in situ salinity data [*Millero and Leung*, 1976]. Alkalinity was derived from a salinity-total alkalinity (A_{Tsalin}) relationship developed for the Chukchi Sea, Beaufort Sea, and Canada Basin [*Yamamoto-Kawai et al*., 2005]. Total dissolved inorganic carbon (DIC) was calculated using the equilibrium program CO2SYS [*van Heuven et al*., 2011] with temperature, salinity, depth, pCO_2, and A_{Tsalin} (protolytic nutrients, e.g., phosphate, were assumed to be negligible) as inputs and returning as outputs DIC and other CO_2 parameters, including $CaCO_3$ saturation. The calculated DIC accuracy is estimated to be ~15 μmol kg^{-1} with a resolution of ~2 μmol kg^{-1}. DO saturation was calculated using in situ temperature, salinity, and barometric pressure [*Gnaiger and Forstner*, 1983]. Atmospheric pCO_2 in water saturated air was calculated by multiplying xCO_2 by local barometric pressure and including water vapor pressure [*Dickson et al*., 2007]. The mixed layer depth (MLD) was calculated from depth-resolved density determined by temperature and salinity measured by the profiling systems. The MLD was defined as the depth where the density difference from the SAMI depth was +0.3 kg m^{-3}. This density difference gives

the best match to the base of the mixed layer based on visual inspection of the density profiles and is close to the value of 0.25 kg m^{-3} found by *Timmermans et al*. [2012] using the same approach for the central Canada Basin.

2.4. Data Validation

An underway pCO_2 equilibrator-infrared measurement system (SUPER-CO_2, Sunburst Sensors, LLC) provided shipboard validation data at the beginning of the deployment. This underway pCO_2 was corrected to the sea surface temperature to account for warming inside the water line and equilibrator. After offsets were applied to the SAMI values, they were further compared to shipboard pCO_2 values collected during the time the ship was at the ITP location. The mean difference ± standard deviation between SAMI and shipboard pCO_2 values were 1.3 ± 0.1 μatm ($n = 3$) for ITP-64 and 0.3 ± 0.3 μatm ($n = 5$) for ITP-65. The profiler DO measured in the mixed layer and SAMI DO data were corrected for any offsets using bottle DO data at the time of the deployment. Bottle DO was determined to within ± 2 μmol kg^{-1} using the Winkler titration method [*Carpenter*, 1965]. The DO values were lower than the Winkler values by 31 μmol kg^{-1} and 23 μmol kg^{-1}, for ITP-64 and ITP-65, respectively. For the remainder of the period, the profiler DO data were corrected for drift by comparing the profiler data with deep-water isopycnal DO data measured at the time of deployment. The DO at these depths does not vary seasonally [*Timmermans et al*., 2010]. The SAMI DO data were then corrected to the surface profiler data whenever the system was in the surface mixed layer. A constant linear drift was observed for ITP-64 and ITP-65 SAMI DO data, accounting for ~-4 μmol kg^{-1} DO drift in both cases. After this correction, the SAMI DO and shallowest ITP profile DO data compared to within ± 0.8 ($n = 97$) μmol kg^{-1} and ± 0.7 ($n = 80$) μmol kg^{-1} for ITP-64 and ITP-65, respectively. Salinity measured by the SAMI and the profiler CTD sensors did not significantly differ and did not require correction.

2.5. Modeling

The variability of DIC and DO was modeled by accounting for contributions from three different fluxes, as shown in equation (1).

$$\mathrm{MLD}\times\rho\times\Delta C/\Delta t = F_{gasex} + F_{NCP} + F_{phys} \quad (1)$$

MLD is the mixed layer depth, ρ is seawater density, ΔC is the difference in DIC or DO concentration (e.g., in μmol kg^{-1}) between two adjacent temporal measurements (Δt), and F_{gasex}, F_{NCP}, F_{phys} are the fluxes due to air-sea gas exchange, net community production (NCP), and all combined physical processes (vertical mixing, horizontal advection, and brine rejection during ice formation), respectively. We assume $CaCO_3$ dissolution and formation were negligible. Using this mass balance approach, it is possible to estimate the overall variability in DIC and DO as we have demonstrated in past marine and freshwater studies [e.g., *DeGrandpre et al*., 1998, 2004; *Baehr and DeGrandpre*, 2004; *Moore et al*. 2011].

The air-sea flux, F_{gasex}, was calculated using the diffusive boundary layer model:

$$F_{gasex} = k \times \Delta C \times f \quad (2)$$

where k is the gas transfer velocity, ΔC is the CO_2 or DO concentration gradient across the air-sea interface, and f is the fraction of open water. k was calculated and adjusted for different temperatures and gases (i.e., CO_2, DO) using the updated wind speed relationship in *Wanninkhof* [2014]. The contribution from complete injection of bubbles to DO supersaturation was modeled using the flux equation in *Stanley et al*. [2009]. Bubble injection of CO_2 was included but is negligible. Other interfacial processes, such as turbulence generated by ice-sea sheer, are not considered here, but could enhance air-sea gas exchange as much as 40% over that predicted with wind speed [*Loose et al*., 2014; *Lovely et al*., 2015]. Wind-driven turbulence is damped in partial ice cover, but the alternative parameterizations are not well established [*Loose et al*., 2014]. We instead evaluate the influence of ice cover using two scenarios: with f in equation (2) equal to the measured value or $f = 1$ (i.e., no ice cover).

F_{NCP} was estimated by computing bandpass-filtered DIC and DO, after removing the contribution of F_{gasex} (calculated from equation (2)). A physiological model was also used to compare to the data-based NCP estimates. DIC and DO data were bandpass-filtered using 4 h low pass and 30 h high pass filters to remove short and long-term fluctuations, respectively. These filtered data were then converted to NCP in terms of mmol m^{-2} d^{-1} using the MLD and density at each time (i.e., the left side of equation (1)). Daily NCP values were calculated by averaging the bandpass-filtered data from dawn to dawn. The daily average, DO-

derived, NCP was compared with NCP derived from DIC by conversion using a photosynthetic quotient (PQ) that assumes production is wholly derived from nitrate consumption (1.4) [*Laws*, 1991]. Data corresponding to time periods where salinity changed rapidly were omitted in the daily mean calculation of NCP as discussed in more detail below.

The physiological model [e.g., *Platt et al*., 1980] used the irradiance (PAR) and biomass (Chl-*a*) dependence of photosynthesis,

$$GPP = P_m^B x \left(1 - e^{-\alpha I / P_m^B}\right) \times e^{-\beta I / P_m^B} Chl{-}a \tag{3}$$

where *GPP* is gross primary production in mg C m^{-3} h^{-1}, P_m^B is the *Chl-a*-specific maximum rate of photosynthesis (mg C mg Chl-a^{-1} h^{-1}), α is the *Chl-a*-specific rate of light-limited photosynthesis (mg C mg Chl-a^{-1} h^{-1} (μmol quanta m^{-2} s^{-1})$^{-1}$), I is the PAR irradiance (μmol quanta m^{-2} s^{-1}), β (same units as α) accounts for photoinhibition, and Chl-*a* is the concentration of chlorophyll-*a* in mg m^{-3} converted to carbon using 0.008 g Chl-*a* per gram C [*Palmer et al*., 2013]. The model used a P_m^B value of 0.20 mg C mg Chl-a^{-1} h^{-1}, an α value of 0.017 mg C mg Chl-a^{-1} h^{-1} (μmol quanta m^{-2} s^{-1})$^{-1}$, and β value of 0.0006 mg C mg Chl-a^{-1} h^{-1} (μmol quanta m^{-2} s^{-1})$^{-1}$ [*Palmer et al*., 2013].

Community respiration (R_1) in mg C m^{-3} h^{-1} was estimated using the following equation:

$$R_1 = R \times \theta_R^{(T+1.46)} \times (GPP \times k_R) \tag{4}$$

where R is the nighttime respiration rate estimated from the rate of change of DO (R_1) during the first night at the mean in situ temperature (−1.46°C), T is the in situ temperature in °C, θ_R is the Arrhenius temperature coefficient (1.045) [*Parkhill and Gulliver*, 1999], and k_R is an empirical proportionality constant (0.23) obtained by a residual sum of squares fit to the DO NCP from the bandpass-filtered data. We observed that with a fixed respiration rate R_1 was significantly overestimated as insolation decreased during the month long-time series. Respiration in the dark Arctic is minimal [*Sherr and Sherr*, 2003] and so we assumed respiration to be proportional to GPP, tightly coupling GPP and respiration as expected in nutrient-depleted waters [*Dugdale and Goering*, 1967]. NCP was then calculated as the difference between *GPP* and R_1.

The combined contribution from purely physical processes such as vertical mixing, horizontal advection, and brine formation, defined here as the sum of the physical fluxes (F_{phys}), was estimated by using a multiple linear least squares analysis based on changes in salinity (S) and *MLD*:

$$\Delta C_{phys} = a \times [MLD_{t2} - MLD_{t1}] + b \times [S_{t2} - S_{t1}] \tag{5}$$

where ΔC_{phys} is the change in DIC or DO concentration due to these physical processes, and a and b are the least squares coefficients for changes in MLD and salinity (measured at 6 m depth), respectively, between two adjacent times t_2 and t_1 (note that F_{phys} in equation (1) is $\Delta C_{phys} \times MLD \times \rho/\Delta t$). To simulate entrainment, the MLD term was computed only when the MLD was observed to deepen. The predictive power in terms of correlation of the modeled and measured parameters was considerably worse if MLD or salinity were used alone, as discussed below.

The individual flux estimates for DIC and DO were included in separate mass balances (equation (1)). The DIC mass balance was integrated into a custom-written program for carbonate system calculations [*DeGrandpre et al*., 2004]. In the program, the DIC is incremented at each time step for contributions from the individual or combined fluxes. The modeled pCO_2 is then calculated from the new DIC, A_{Tsalin}, temperature, and salinity. Because the program calculates the inorganic carbon equilibria and solubility constants using the in situ temperature, the effects of heating and cooling on the pCO_2 are intrinsic in the model. A similar approach was used in the DO model, but as DO exists in only one dissolved form, the DO modeling was comparatively simpler. Both pCO_2 and DO gas exchange models were also calculated assuming ice-free conditions, with the goal to show the extent to which AO ice coverage limits CO_2 and DO air-sea exchange.

3. Results

The 49 and 41 day time series data for ITP-64 and ITP-65, respectively, are shown in Figure 2. The time series from the SAMI sensors ended when the inductive modem communications inexplicably failed, while the

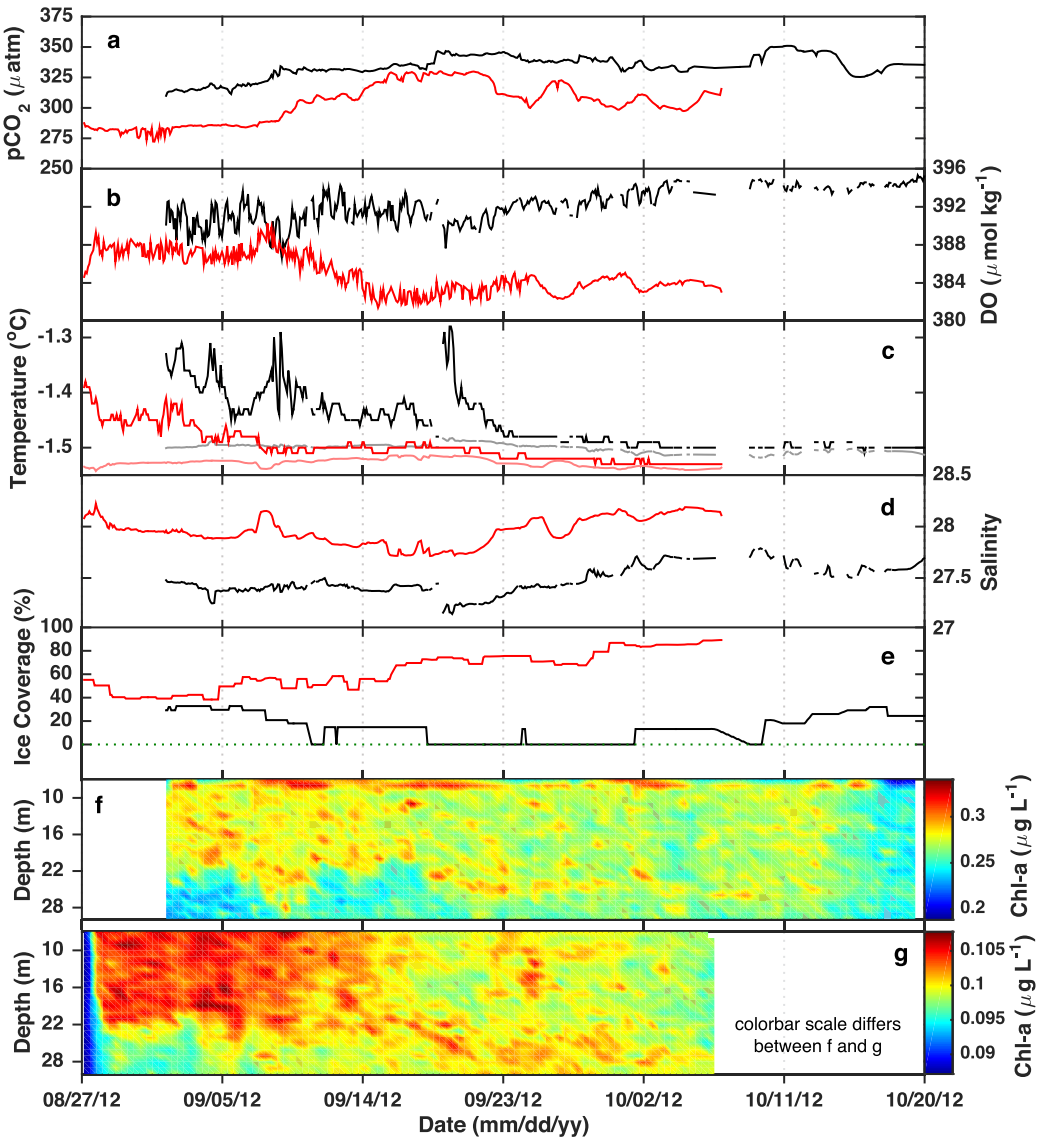

Figure 2. (a–d) Biogeochemical and physical time series data collected at ~6 m depth on ITP-64 (black) and ITP-65 (red). (e) ITP-64 was deployed under little ice whereas ITP-65 was deployed under multi-year ice. Gaps in the data correspond to instrument communication dropouts. (d) The gray and light red lines in the temperature plot refer to freezing temperature of water at ITP-64 and ITP-65, respectively. (f-g) Chl-a profile data from ITP-64 (f) and ITP-65 (g). Note that the colorbar scale changes from Figures 2f to 2g.

profiling units continued to operate. The fixed instruments likely continued operating as well, although no additional surface data were obtained because the ITPs are not typically recovered. Corresponding physical data are shown in Figures 2 and 3. Mean values are summarized in Table 1. The pCO_2 was well below atmospheric saturation for both locations. ITP-64 pCO_2 ranged from 310 to 351 μatm with a mean of 334 ± 9 μatm, and ITP-65 ranged from 272 to 330 μatm with a mean of 304 ± 16 μatm (Figure 2a). DO records showed little variability in either time series (Figure 2b) with levels similar to those found by *Timmermans et al*. [2010]. Note that small amplitude diel cycles are distinct early on in the DO data from ITP-64 (Figure 2b), but are not as clearly apparent in the ITP-65 DO record (Figure 2b). Diel cycles in DIC at ITP-64 are also evident once the long-term trend is removed with a bandpass filter (see below).

The ice cover near ITP-64 ranged from 0 to 33% with a mean of 14 ± 12% (Figure 2e); whereas, ITP-65 ice cover ranged from 38 to 89% with a mean of 63 ± 16%. Temperatures measured by the 6 m MicroCAT interfaced with ITP-64 were slightly higher than those seen with ITP-65, until they converged towards the freezing point around 21 September (Figure 2c). There was a significant difference in salinity between the two

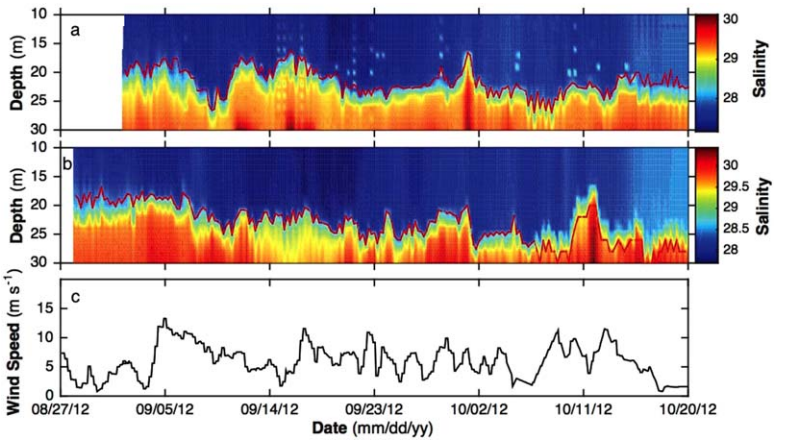

Figure 3. Depth-time plots of salinity from (a) ITP-64 and (b) ITP-65 profiler data. Red contour lines indicate the base of the mixed layer. (c) The wind speed is shown.

ITPs, with ITP-64 and ITP-65 exhibiting mean salinities of 27.5 ± 0.1 and 28.0 ± 0.1 at 6 m, respectively (Table 1) (Figure 2d). Over most of the measurement period, Chl-*a* at ITP-64 was ~3 times higher (~0.3 μg L^{-1}) than ITP-65 (Figures 2f, 2g, and Table 1). Both chlorophyll time series exhibited decreasing concentrations in the upper 30 m over the observational period, suggesting end-of-season decreases in photosynthetic biomass. Mean MLD was ~22 m at both locations (Figure 3 and Table 1). Wind speed ranged from 0.8 to 13.3 m s^{-1} with a mean of 6.2 ± 2.7 m s^{-1} (Figure 3c). The atmospheric xCO_2 measured at Barrow, Alaska ranged from 375 to 405 μatm with a mean of 386 ± 6 μatm (time series data not shown).

4. Discussion

4.1. Comparisons of In Situ Data and Model Estimates

4.1.1. ITP-64 (Low Sea Ice Cover)

Results from the biogeochemical models are compared with the observed, in situ pCO_2 and DO time series (Figure 4). The pCO_2 trend predicted due to gas exchange generally follows the upward trend in the time series data but continues to rise after late September whereas the time series level off and show large (10–20 μatm) rapid changes. With no ice present, the pCO_2 initially increased more rapidly (blue dashed curve in Figure 4) but then the ice and no-ice estimates stopped diverging as ice cover disappeared by mid-September (Figure 2e). As stated earlier, temperature effects on pCO_2 are included in the mass balance model. In most ocean regions, temperature changes are an important contributor to pCO_2 variability, but the ~0.2°C drop in temperature observed here (Figure 2c) corresponds to only a ~2.5 μatm decrease in pCO_2. DO gas exchange without bubbles predicts that DO would quickly reach atmospheric equilibrium

Table 1. Mean Parameter Values ± Standard Deviation From ITP-64 and ITP-65 Locations[a]

Parameter	ITP-64	ITP-65	Mean Difference (ITP-64 – ITP-65)	Measurement Source
Ice coverage (%)	14 ± 12	63 ± 16	−49	NSIDC
Temperature (°C)	−1.46 ± 0.05	−1.50 ± 0.03	0.04	MicroCAT (~6 m)
Salinity	27.5 ± 0.1	28.0 ± 0.1	−0.5	MicroCAT (~6 m)
Mixed layer depth (m)	21.5 ± 2.1	22.0 ± 2.5	−0.5	Profiler
pCO_2 (μatm)	334 ± 9	304 ± 16	30	SAMI (~6 m)
ΔpCO_2 (μatm)	−51.6 ± 9.5	−80.0 ± 15	−28.4	Calculated
CO_2 flux (mmol m^{-2} d^{-1})	−4.8 ± 3.8	−2.5 ± 2.6	2.3	Calculated
DO (μmol kg^{-1})	392 ± 2	385 ± 2	7.4	Optode (~6 m)
ΔDO (% saturation)	3.0 ± 0.1	1.3 ± 0.1	1.7	Calculated
DO flux (mmol m^{-2} d^{-1})	15.6 ± 13	2.2 ± 2.7	13.4	Calculated
Chl-*a* (μg L^{-1})	0.28 ± 0.01	0.100 ± 0.002	0.18	Profiler
NCP (mmol C m^{-2} d^{-1})	3.5 ± 30	0.0± 23	3.5	Calculated
Ω_{arag} (unitless)	1.00 ± 0.02	1.12 ± 0.06	−0.12	Calculated

[a]The right-most column indicates the data source.

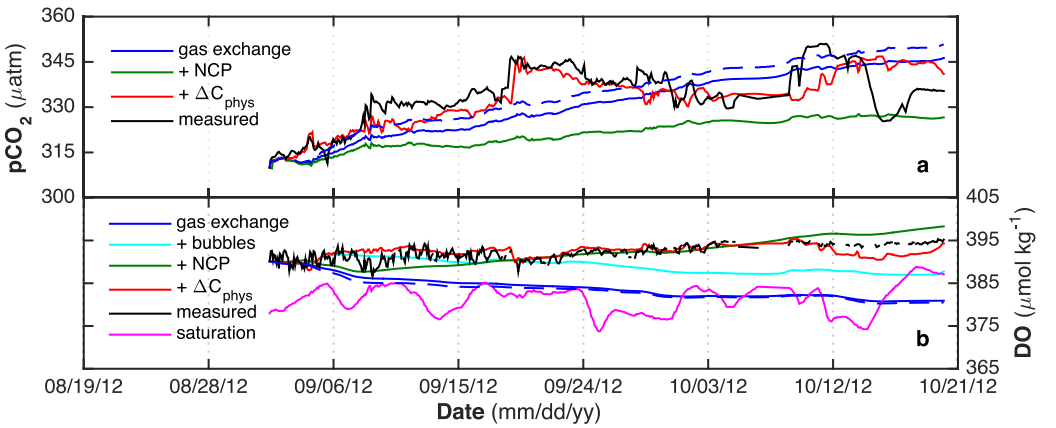

Figure 4. (a and b) ITP-64 pCO_2 and DO observations (black, respectively) and modeled contributions from the following individual and combined processes: air-sea gas exchange with ice cover (blue), including bubble injection (cyan, DO only), including NCP (green), and including physical processes as defined in equation (5) (red). Gas exchange with no ice cover is shown as blue-dashed curves (omitted from the legends due to lack of space). DO at 100% saturation is also shown (magenta).

(Figure 4b) and, based on the no-ice model, that the minimal ice cover had no significant effect on the DO levels. The DO data are significantly higher than saturation, however. Including bubble injection in the gas exchange model accounts for some of the observed DO supersaturation.

The gas exchange models over and under estimate pCO_2 and DO in late September, respectively. These divergences could originate from net biological production (positive NCP) because, in this case, it would counteract the loss of DO and gain of CO_2 from gas exchange. Initially there was significant production, evident in the diel cycle of DO (Figure 2b) but this diel signal slowly diminished and finally disappeared in early

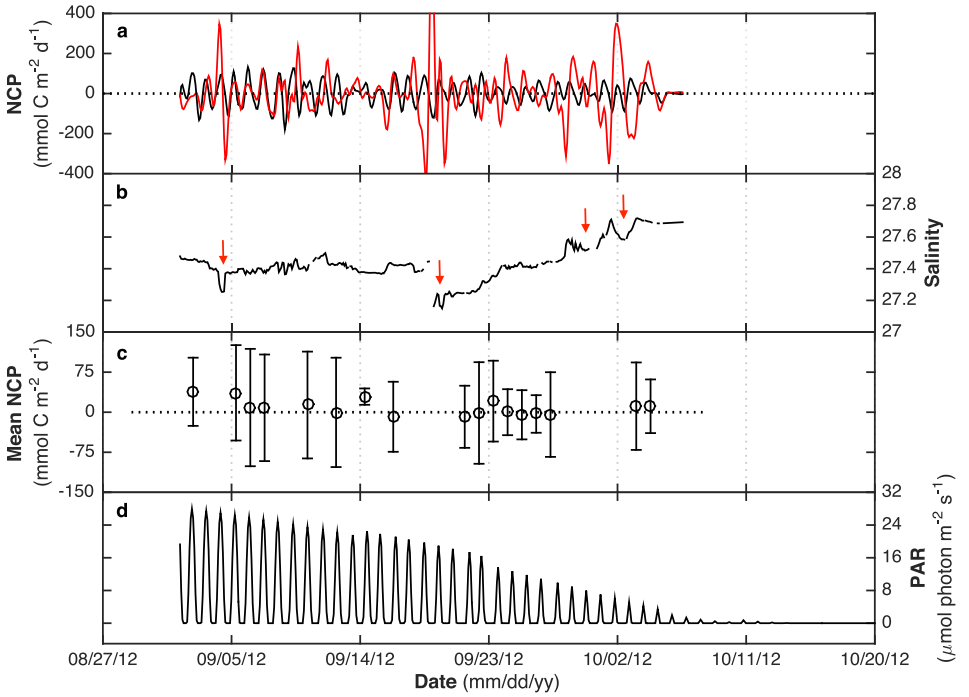

Figure 5. (top) NCP from the bandpass filtered DIC (red) and DO (black) ITP-64 data. DIC NCP was multiplied by −1 to make NCP positive during periods of net photosynthesis. Abrupt changes in salinity (highlighted by downward arrows) indicate potential advection of waters with different levels of pCO_2 and DO. Daily mean (open circle) ± standard deviation of NCP based on DO is shown in the third plot. The mean was calculated over a 24 h period starting at 8 A.M. local time with the periods omitted when salinity was significantly changing. The PAR data were calculated from the incident solar radiation that was initially scaled using the surface PAR data collected on the ship (see Methods).

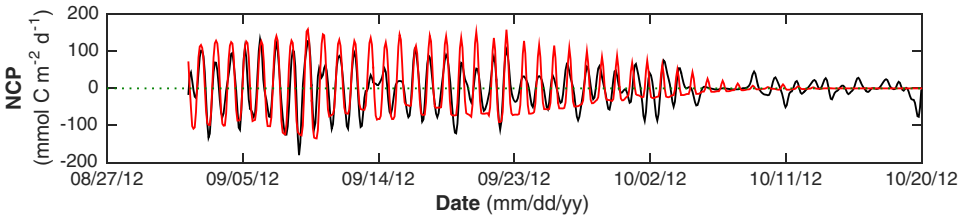

Figure 6. ITP-64 NCP calculated from equations (3) and (4) (red), and NCP calculated from in situ bandpass-filtered DO (black, same data as shown in Figure 5). After 26 September, NCP from DO and modeled NCP became increasingly smaller as day length approached zero (see PAR, Figure 5).

October. This diel behavior becomes more evident in the bandpass-filtered time series of DO and CO_2 (shown as NCP in Figure 5a). The NCP from DO and DIC closely match during some periods within these time series (e.g., correlating with an r^2 of 0.72 from 4 to 9 September), but at times the DIC exhibited a much larger-amplitude oscillation. These larger-amplitude times correspond to periods when salinity rapidly changed (Figure 5b, arrows) suggesting that water mass changes around the ITP location played a role in these perturbations. This non-Redfield variability of CO_2 and DO may be due to advection of a past production signal where the DO produced from photosynthesis more rapidly equilibrated with the atmosphere leaving behind a residual CO_2 undersaturation [*DeGrandpre et al.*, 1998]. Consequently, when water masses moved by the sensors, the DO did not vary as much as the pCO_2 (or DIC) and these appear as large oscillations in the DIC NCP (Figure 5a). Omitting these periods when salinity was changing rapidly, the mean daily NCP is 4.9 mmol O_2 m^{-2} d^{-1} (or 3.5 mmol C m^{-2} d^{-1}) (Figure 5c).

The bandpass-filtered NCP data calculated from in situ DO are compared with the photosynthetic model (equations (3) and (4)) in Figure 6. The model reproduced the DO NCP reasonably well ($r^2 = 0.60$) with a mean NCP of 3.0 mmol C m^{-2} d^{-1}. Some of the day-to-day mismatches are likely due to inaccuracy of the PAR irradiance due to locally variable ice and cloud cover. These results support that local NCP was driving the observed diel variability. Using the mean bandpass-derived NCP from Figure 6 of 3.5 mmol C m^{-2} d^{-1} gives a total DO and DIC change of 10 and 7 μmol kg^{-1} respectively, over the time series period. Samples obtained at the time of deployment at 6 and 20 m had 0.2 and 2.0 μmol kg^{-1} nitrate, respectively. Assuming a mean mixed layer value of 1.1 μmol kg^{-1}, complete uptake of the nitrate would result in changes close to those observed for DO and DIC using the Redfield stoichiometry for O_2:NO_3:CO_2 of 138:100:16. This nitrate may have arisen from upwelling along the ice edge [*Gammelsrød et al.*, 1975] or earlier vertical entrainment due to high winds over the open water where ITP-64 was deployed.

The NCP estimated from DO (4.9 mmol O_2 m^{-2} d^{-1}) was considered the most accurate estimate of local NCP because it was not as strongly affected by past production signals as in the case of DIC. Using this mean NCP combined with diffusive and bubble gas exchange, gives a reasonable fit to the O_2 data ($r^2 = 0.6$) until 9 October when the model overestimates the DO (Figure 4b). This NCP, adjusted for the PQ (1.4) in the pCO_2 model (3.5 mmol C m^{-2} d^{-1}), combined with gas exchange gives much lower pCO_2 levels than observed, however (Figure 4a).

As discussed above, some of these large changes in pCO_2 are not mirrored in the DO record and these divergent periods are likely related to advection of horizontal features. We used the least squares analysis (equation (5)) to estimate the importance of these and other physical processes. This analysis explains a significant portion of the pCO_2 variability not accounted for by gas exchange + NCP (Figure 4a and Table 2). The model fit to DO also slightly improves (Table 2) with subtle baseline shifts now accounted for by the model (Figure 4b). Salinity is considerably more weighted than MLD even though they have similar means and variance (Table 1) but the prediction worsened if either parameter was used alone and more so if only MLD was used. Salinity and MLD were not significantly correlated indicating that the two parameters explain different sources of variability. These results are not supportive of substantial vertical entrainment (due to convection from sea ice growth

Table 2. Coefficients From the Least Squares Fit Between the Model and Data (Figures 4 and 8)

	Species	a (MLD)	b (Salinity)	[a]r^2	[b]r^2
ITP-64	pCO_2	0.129	42.4	0.39	0.55
	DO	0.019	11.6	0.15	0.22
ITP-65	pCO_2	0.0441	33.5	0.33	0.88
	DO	−0.031	4.88	0.46	0.70

[a] and [b] are the correlations without and with ΔC_{phys}, respectively.

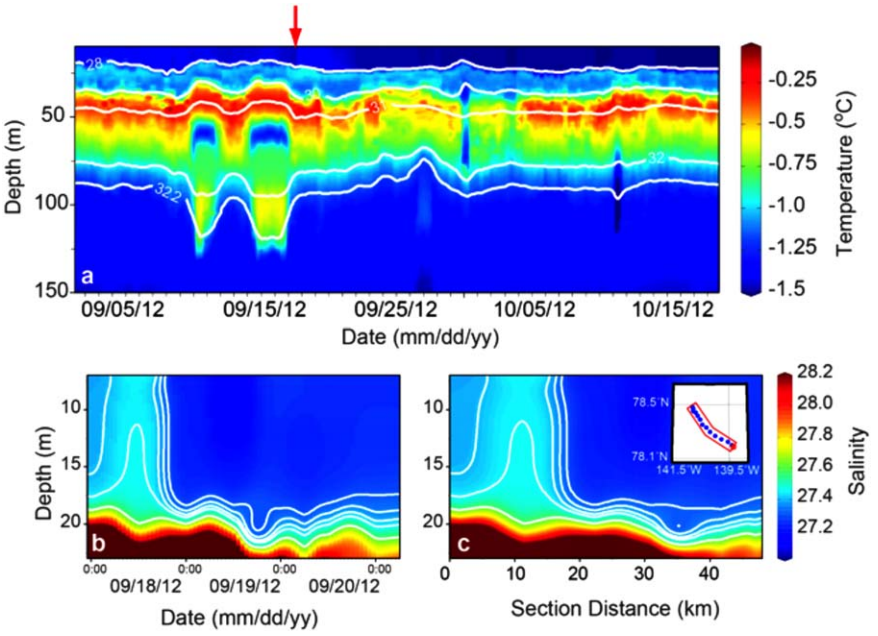

Figure 7. (a) ITP-64 temperature and depth time series with salinity contours (effectively also showing density variations because of the weak density dependence on temperature at these low temperatures). A range of eddy features are present, indicated by isohaline/isopycnal displacements. (b) A close-up section of mixed layer salinity centered on the location marked by the red arrow in Figure 7a. This corresponds to the second red arrow from the left in Figure 5b. At this point, the ITP drifted across a surface front in salinity that appears to be also related to a brief deviation to mixed layer temperatures above the freezing point (Figure 2) (potentially a result of entrainment at the base of the mixed layer). (c) The depth-time section (left) does not differ significantly from a depth-distance section (with profile locations marked in the inset map) and shows the spatial scale of the feature (assuming it did not evolve significantly during the ITP drift).

or shear-driven mixing) but suggest a greater importance for horizontal gradients. While there is significant mixed layer variability (Figure 3), these are mostly related to mesoscale heaving (induced by sub mixed layer eddies), combined with spatial variability as the ITPs drifted. There is some evidence for shear-driven mixing, i.e., the deepening of the mixed layer during the high wind event on 5 September (Figure 3), but these events do not seem to add up to much over the entire time-series, reflecting the difficulty in mixing the strong halocline in this region. The ITP-64 temperature and salinity measurements (Figure 2) show a range of eddies and ocean fronts (see expanded view in Figure 7). *Eveleth et al*. [2014] found that the surface AO shows horizontal variability on short spatial scales (~1 km) that can be attributed to surface-ocean fronts and mixing processes in the vicinity of these fronts.

Ice formation or melting would also correlate with salinity. Local ice formation could have started around ~9 September when water reached the freezing point (Figure 2c). Salinity began to slowly increase around this time with a ~1.5% net increase until 3 October when it leveled off (Figure 2d). Ice formation could have increased the mixed layer DO by ~3 μmol kg^{-1} during this period assuming 100% of the salinity and 50% of the DO was rejected from the ice [*Crabeck et al*., 2014; *Loose et al*., 2009]. DO has a small upward trend during this time, which could be due to this process. The effect on inorganic carbon is more difficult to estimate because studies have found that variable amounts of DIC and A_T are retained in ice and the DIC/A_T ratio changes [*Rysgaard et al*., 2007; *Miller et al*., 2011]. The ratio depends upon ice type, formation rate, temperature, and other parameters. If DIC and A_T both increased in proportion to salinity, the pCO_2 would have increased by only ~7 μatm because pCO_2 changes are small when the DIC and A_T change in the same proportion. However, high pCO_2 levels are often observed during ice formation because A_T is preferentially retained in the ice leading to an increased DIC/A_T ratio in the water [*Rysgaard et al*., 2007]. However, the pCO_2 actually decreases during this period. Horizontal gradients, as discussed above, likely mask any local signal from ice production.

4.1.2. ITP-65 (Substantial Sea Ice Cover)

The model results for the ITP-65 data are shown in Figure 8. The contribution from gas exchange to the ITP-65 pCO_2 is small, but would be significantly larger if no ice was present (Figure 8a). The model predicts that diffusional gas exchange would keep the DO near saturation but raises slightly above saturation with

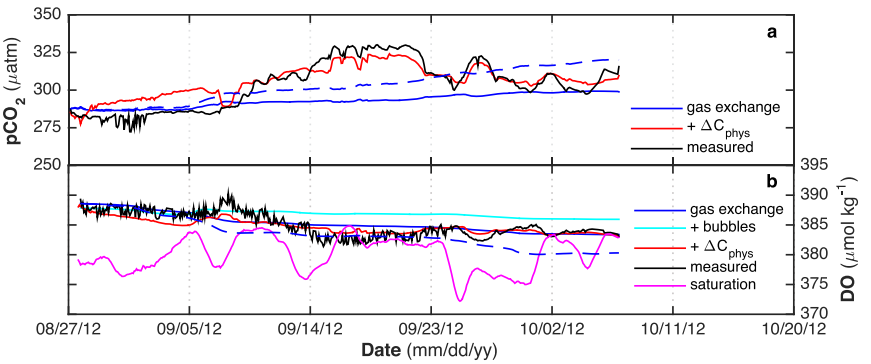

Figure 8. ITP-65 pCO_2 and DO data and modeled time series. The description is the same as Figure 4. NCP was negligible for ITP-65 and was not included in the modeling analysis.

bubble injection. The lack of a diel cycle in the bandpass filtered data (not shown) suggests that NCP did not significantly contribute to the variability. Low light levels under multiyear ice are unlikely to support significant production, there was no detectable nitrate for new production in the mixed layer at the time of deployment, and phytoplankton biomass was low, with Chl-*a* concentrations almost 3 times smaller than observed at ITP-64. Much of the remaining DO variability can be explained using the salinity and ML least squares fit (Table 2) with the r^2 increasing to 0.70 (Table 2).

As shown in Figure 8a, there are some large pCO_2 changes (around 10 and 26 September and 2 October) that gas exchange could not explain. Many of these changes are related to mixing, water mass changes, and/or ice formation ($r^2 = 0.88$, Table 2). The combined physical model explained more of the observed variability than at the ITP-64 locations (Table 2) indicating the greater importance of these physical processes under ice. The drift track of ITP-65 in the vicinity of 80°N passed through water-mass structures as it transitioned from a Canada Basin water mass in the south (with strong Pacific influence) to Eurasian water in the north [see e.g., *Timmermans et al.*, 2008] (Figure 9). These changes are associated with a north-south gradient in surface salinity with fresher surface waters toward the Beaufort Gyre, as observed in the ITP-65 drift (Figure 2), although with some temporal increase in salinity as sea ice likely began to grow in the latter half of September. As ITP-65 drifted south, the large-scale gradient transitioned to higher pCO_2 and lower DO (Figure 9) with physical and biological controls on pCO_2 and DO superimposed on this gradient. Much of the changes in pCO_2 that cannot be explained by gas exchange appear to be a consequence of instrument

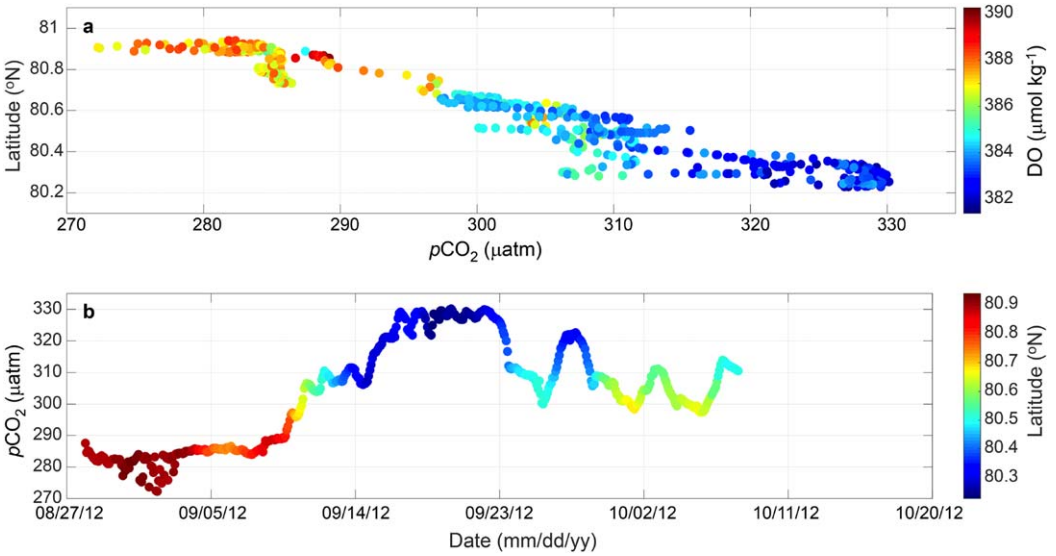

Figure 9. (a) ITP-65 pCO_2 and DO versus latitude, and (b) pCO_2 time series with latitude shown as color.

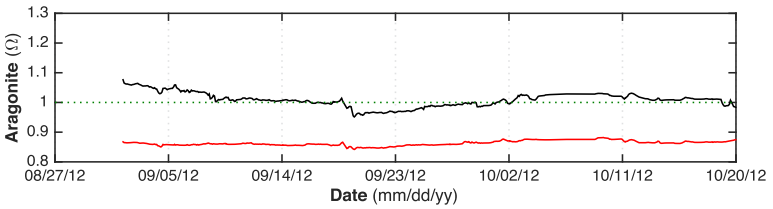

Figure 10. Aragonite saturation state (Ω_{arag}) at ITP-64. The black solid line refers to Ω_{arag} under current conditions. The dotted line represents aragonite at saturation. The red line refers to Ω_{arag} when the surface of the AO is in equilibrium with atmospheric pCO_2. Equilibrium between seawater and the atmosphere brings Ω_{arag} consistently below 1, favoring continuous aragonite dissolution.

drift to the south, with increasing and then decreasing pCO_2 when the system drifts south and then north (Figure 9b). The overall north-south property gradients are not a prominent feature of ITP-64 measurements, in contrast.

4.2. Ocean Acidification

The model indicates that uptake of atmospheric CO_2 was significant in the open water region. It is apparent that if open water periods continue to increase the sea surface pCO_2 in the deep ocean basins will increase towards atmospheric saturation, perhaps eventually reaching mean levels similar those in other oligotrophic ocean regions [*Bates et al*., 2014]. Increased CO_2 will decrease pH and carbonate ion concentrations and therefore decrease calcium carbonate saturation levels. We calculated aragonite saturation (Ω_{arag}) at present pCO_2 levels and at atmospheric saturation (assuming atmospheric pCO_2 at 400 μatm) using the A_{Tsalin} and in situ temperature and salinity in CO2SYS. Under the low-ice conditions at ITP-64, Ω_{arag} had a mean of 1.00 ± 0.02 with Ω_{arag} being below 1 at times (Figure 10). Under atmospheric equilibrium conditions, the mean was 0.86 ± 0.01 (Figure 10); therefore, with sustained open water, equilibrium of AO surface water with the atmosphere will bring Ω_{arag} consistently below 1, favoring continuous aragonite dissolution. Undersaturation of the surface waters of the Canada Basin with respect to aragonite has already been observed [*Yamamoto-Kawai et al*., 2009b]. Since the preindustrial period, the increase in atmospheric CO_2, surface water warming, and melting of sea ice has lowered surface calcium carbonate saturation state in the Canada Basin by ~0.3, 0.1, and 0.4 units, respectively [*Yamamoto-Kawai et al*., 2011]. Under such conditions, the calcium carbonate shells of many marine organisms will dissolve.

5. Conclusions

We estimate NCP to have been 3.5 and ~0 mmol C m^{-2} d^{-1} in this region of the AO, under partial and multiyear ice cover, respectively, during this part of the growing season. In 2002, *Bates et al.* [2005] estimated NCP based on DIC inventories during spring and summer in the Canada Basin to be 1.3–2.1 mmol C m^{-2} d^{-1} while the NCP in shelf regions was dramatically higher (80–240 mmol C m^{-2} d^{-1}). *Ulfsbo et al.* [2014] reported NCP values of 2–7 mmol C m^{-2} d^{-1} based on underway pCO_2 measurements in the ice-covered deep Canada Basin during late August of 2011. While ice algae at the ice-sea interface could contribute to the overall production, it has been estimated to be small compared to the pelagic signal [*Arrigo and van Dijken*, 2015].

The comparison between the pCO_2 and DO from the two ITPs indicate that insufficient availability of light and nutrients limits production in the AO. Even with open water conditions NCP remained very low in the Canada Basin, but it did contribute significantly to the observed trends in pCO_2 and DO (Figure 4). The NCP was comparable to the air-sea flux at ITP-64 (Table 1) and therefore significantly offset the increase in CO_2 that would have otherwise occurred. Horizontal gradients dominated pCO_2 variability in the densely ice-covered region with small uptake due to gas exchange and negligible NCP in the surface. The surface gradients are in part a manifestation of the complicated upper ocean flows in addition to the circuitous drift tracks of the ITPs over larger-scale property gradients.

Others have predicted that production in the AO surface mixed layer will be reduced in the future as increasing freshwater from ice melt inhibits the entrainment of subsurface nutrients [*Pabi et al*., 2008]. The carbon cycle consequences due to reduced production would be significant as the pCO_2 in an ice-free AO will continue towards atmospheric saturation if not offset by primary production [*Cai et al*. 2010]. This leads to a decreasing carbon uptake from the atmosphere while accelerating ocean acidification at the same

time. Continued monitoring of pCO_2 in the Canada Basin will be necessary to verify if a trend is present and to what extent pCO_2 levels are modified by other processes that are also changing (e.g., ice coverage, surface warming, and NCP).

Acknowledgments
We thank Kris Newhall, Steve Lambert, Jim Dunne, and Jeff O'Brien from Woods Hole Oceanographic Institution, Jim Beck from Sunburst Sensors, and Brittany Peterson from the University of Montana. Rachel Stanley provided helpful discussions regarding bubble injection. We also thank the captain, officers, crew, and chief scientist (Bill Williams) of the *CCGS Louis S. St. Laurent* during the 2012 Canadian Joint Ocean Ice Study in collaboration with the Beaufort Gyre Observing System project (www.whoi.edu/beaufortgyre). Funding was provided by the U.S. National Science Foundation Arctic Observing Network (ARC-1107346 and ARC-0856479). Data from this study can be accessed at https://arcticdata.io.

References

Anderson, L. G., and S. Kaltin (2001), Carbon fluxes in the Arctic Ocean: Potential impact by climate change, *Polar Res.*, *20*, 225–232.
Anderson, L. G., S. Jutterstrom, S. H. Hjalmarsson, I. Wahlstrom, and I. P. Semiletov (2009), Out-gassing of CO_2 from Siberian Shelf seas by terrestrial organic matter decomposition, *Geophys. Res. Lett.*, *36*, L20601, doi:10.1029/2009GL040046.
Arrigo, K. R., and G. L. van Dijken (2015), Continued increases in Arctic Ocean primary production, *Prog. Oceanogr.*, *136*, 60–70, doi:10.1016/j.pocean.2015.05.002.
Baehr, M. M., and M. D. DeGrandpre (2004), In situ pCO_2 and O_2 measurements in a freshwater lake during turnover and stratification: Observations and a model, *Limnol. Oceanogr.*, *49*, 330–340.
Bates, N. R. (2006), Air-sea carbon dioxide fluxes and the continental shelf pump of carbon in the Chukchi Sea adjacent to the Arctic Ocean, *J. Geophys. Res.*, *111*, C10013, doi:10.1029/2005JC003083.
Bates, N. R., Margaret H. P. B., and D. A. Hansell (2005), Spatio-temporal distribution of dissolved inorganic carbon and net community production in the Chukchi and Beaufort Seas, *Deep Sea Res., Part II*, *52*, 3303–3323, doi:10.1016/j.dsr2.2005.10.005.
Bates, N. R., S. B. Moran, D. A. Hansell, and J. T. Mathis (2006), An increasing CO_2 sink in the Arctic Ocean due to sea-ice loss, *Geophys. Res. Lett.*, *33*, L23609, doi:10.1029/2006GL027028.
Bates, N. R., Y. M. Astor, M. J. Church, K. Currie, J. E. Dore, M. González-Dávila, L. Lorenzoni, F. Muller-Karger, J. Olafsson, and J. M. Santana-Casiano (2014), A time-series view of changing ocean chemistry due to ocean uptake of anthropogenic CO_2 and ocean acidification, *Oceanography*, *27*, 126–141, doi:10.5670/oceanog.2014.16.
Cai, W., et al. (2010), Decrease in the CO_2 uptake capacity in an ice-free Arctic Ocean basin, *Science*, *329*, 556–559, doi:10.1126/science.1189338.
Carpenter, J. H. (1965), The Chesapeake Bay Institute technique for the Winkler dissolved oxygen method, *Limnol. Oceanogr.*, *10*, 141–143.
Crabeck, O., B. Delille, S. Rysgaard, D. N. Thomas, N.-X. Geilfus, B. Else, and J.-L. Tison (2014), First "in situ" determination of gas transport coefficients (D_{O2}, D_{Ar}, and D_{N2}) from bulk gas concentration measurements (O_2, N_2, Ar) in natural sea ice, *J. Geophys. Res. Oceans*, *119*, 6655–6668, doi:10.1002/2014JC009849.
DeGrandpre, M. D., T. R. Hammar, S. P. Smith, and F. L. Sayles (1995), In situ measurements of seawater pCO_2, *Limnol. Oceanogr.*, *40*, 969–975.
DeGrandpre, M. D., T. R. Hammar, and C. D. Wirick (1998), Short term pCO_2 and O_2 dynamics in California coastal waters, *Deep Sea Res., Part II*, *45*, 1557–1575.
DeGrandpre, M. D., R. Wanninkhof, W. R. McGillis, and P. Strutton (2004), A Lagrangian study of pCO_2 dynamics in the eastern equatorial Pacific Ocean, *J. Geophys. Res.*, *109*, C08S07, doi:10.1029/2003JC002089.
Dickson, A. G., C. L. Sabine, and J. R. Christian (Eds.) (2007), *Guide to Best Practices for Ocean CO_2 Measurements*, *PICES Spec. Publ.*, *3*, 191 pp.
Dugdale, R. C., and J. J. Goering (1967), Uptake of new and regenerated forms of nitrogen in primary productivity, *Limnol. Oceanogr.*, *12*, 196–207.
Else, G. T., R. J. Galley, B. Lansard, D. G. Barber, K. Brown, L. A. Miller, A. Mucci, T. N. Papakyriakou, J.-É. Tremblay, and S. Rysgaard (2013), Further observations of a decreasing atmospheric CO_2 uptake capacity in the Canada Basin (Arctic Ocean) due to sea ice loss, *Geophys. Res. Lett.*, *40*, 1132–1137, doi:10.1002/grl.50268.
Eveleth, R., M.-L. Timmermans, and N. Cassar (2014), Physical and biological controls on oxygen saturation variability in the upper Arctic Ocean, *J. Geophys. Res. Oceans*, *119*, 7420–7432, doi:10.1002/2014JC009816.
Evans, W., et al. (2015), Sea-air CO_2 exchange in the western Arctic coastal ocean, *Global Biogeochem. Cycles*, *29*, 1190–1209, doi:10.1002/2015GB005153.
Frey, K. E., D. K. Perovich, and B. Light (2011), The spatial distribution of solar radiation under a melting Arctic sea ice cover, *Geophys. Res. Lett.*, *38*, L22501, doi:10.1029/2011GL049421.
Gammelsrød, T., M. Mork, and L. P. Røed (1975), Upwelling possibilities at an ice edge: Homogeneous model, *Mar. Sci. Commun.*, *1*, 115–145.
Gnaiger, E., and H. Forstner (1983), *Polarographic Oxygen Sensors: Aquatic and Physiological Applications*, 326 pp., Springer, Berlin, Heidelberg, New York.
Gray, S. E., M. D. DeGrandpre, T. M. Moore, T. R. Martz, G. E. Friederich, and K.S. Johnson (2011), Applications of in situ pH measurements for inorganic carbon calculations, *Mar. Chem.*, *125*, 82–90.
Islam, F., M. DeGrandpre, C. Beatty, R. Krishfield, and J. Toole (2016), Gas exchange of CO_2 and O_2 in partially ice-covered regions of the Arctic Ocean investigated using in situ sensors, *IOP Conf. Ser. Earth Environ. Sci.*, *35*, 1–7, doi:10.1088/1755-1315/35/1/012018.
Itoh, M., E. Carmack, K. Shimada, F. McLaughlin, S. Nishino, and S. Zimmermann (2007), Formation and spreading of Eurasian source oxygen-rich halocline water into the Canadian Basin in the Arctic Ocean, *Geophys. Res. Lett.*, *34*, L08603, doi:10.1029/2007GL029482.
Jutterström, S., and L. G. Anderson (2010), Uptake of CO_2 by the Arctic Ocean in a changing climate, *Mar. Chem.*, *122*, 96–104.
Kaltin, S., and L. G. Anderson (2005), Uptake of atmospheric carbon dioxide in Arctic shelf seas: Evaluation of the relative importance of processes that influence pCO_2 in water transported over the Bering- Chukchi Sea shelf, *Mar. Chem.*, *94*, 67–79.
Krishfield, R., J. Toole, A. Proshutinsky, and M.-L. Timmermans (2008), Automated ice-tethered profilers for seawater observations under pack ice in all seasons, *J. Atmos. Ocean. Technol.*, *25*, 2091–2105, doi:10.1175/2008JTECHO587.1.
Krishfield, R. A., A. Proshutinsky, K. Tateyama, W. J. Williams, E. C. Carmack, F. A. McLaughlin, and M.-L. Timmermans (2014), Deterioration of perennial sea ice in the Beaufort Gyre from 2003 to 2012 and its impact on the oceanic freshwater cycle, *J. Geophys. Res. Oceans*, *119*, 1271–1305, doi:10.1002/2013JC008999.
Laney, S. R., R. A. Krishfield, J. M. Toole, T. R. Hammar, C. J. Ashjian, and M.-L. Timmermans (2014), Assessing algal biomass and bio-optical distributions in perennially ice-covered polar ocean ecosystems, *Polar Sci.*, *8*, 73–85.
Laws, E. A. (1991), Photosynthetic quotients, new production and net community production in the open ocean, *Deep Sea Res., Part A*, *38*, 143–167.
Long, M. C., K. Lindsay, and M. M. Holland (2015), Modeling photosynthesis in sea ice-covered waters, *J. Adv. Model. Earth Syst.*, *7*, 1189–1206, doi:10.1002/2015MS000436.
Loose, B., W. R. McGillis, P. Schlosser, D. Perovich, and T. Takahashi (2009), Effects of freezing, growth, and ice cover on gas transport processes in laboratory seawater experiments, *Geophys. Res. Lett.*, *36*, L05603, doi:10.1029/2008GL036318.

Loose B., W. R. McGillis, D. Perovich, C. J. Zappa and P. Schlosser (2014), A parameter model of gas exchange for the seasonal sea ice zone, *Ocean Sci.*, *10*, 17–28.

Lovely, A., B. Loose, P. Schlosser, W. McGillis, C. Zappa, D. Perovich, S. Brown, T. Morell, D. Hsueh, and R. Friedrich (2015), The Gas Transfer through Polar Sea ice experiment: Insights into the rates and pathways that determine geochemical fluxes, *J. Geophys. Res. Oceans*, *120*, 8177–8194, doi:10.1002/2014JC010607.

Maslanik, J.A., C. Fowler, J. Stroeve, S. Drobot, J. Zwally, D. Yi, and W. Emery (2007), A younger, thinner Arctic ice cover: Increased potential for rapid, extensive sea-ice loss, *Geophys. Res. Lett.*, *34*, L24501, doi:10.1029/2007GL032043.

McLaughlin, F., E. Carmack, A. Proshutinsky, R.A. Krishfield, C. Guay, M. Yamamoto-Kawai, J. M. Jackson, and B. Williams (2011), The rapid response of the Canada Basin to climate forcing: From bellwether to alarm bells, *Oceanography*, *24*, 146–159, doi.org/10.5670/oceanog.2011.66.

Miller, L. A., G. Carnat, B. G. T. Else, N. Sutherland, and T. N. Papakyriakou (2011), Carbonate system evolution at the Arctic Ocean surface during autumn freeze-up, *J. Geophys. Res.*, *116*, C00G04, doi:10.1029/2011JC007143.

Millero, F. J., and W. H. Leung (1976), The thermodynamics of seawater at one atmosphere, *Am. J. Sci.*, *276*, 1035–1077.

Moore, T. S., M. D. DeGrandpre, C. L. Sabine, C. J. Zappa, W. R. McGillis, R. A Feely, R. C. Hamme, and W. M. Drennan (2011), Sea surface pCO_2 and O_2 in the Southern Ocean during the austral fall, 2008, *J. Geophys. Res.*, *116*, C00F11, doi:10.1029/2010JC006560.

Murata, A., and T. Takizawa (2003), Summertime CO_2 sinks in shelf and slope waters of the western Arctic Ocean, *Cont. Shelf Res.*, *23*, 753–776.

Pabi, S., G. L. van Dijken, and K. R. Arrigo (2008), Primary production in the Arctic Ocean, 1998-2006, *J. Geophys. Res.*, *113*, C08005, doi:10.1029/2007JC004578.

Palmer, M. A., G. L. van Dijken, B. G. Mitchell, B. J. Seegers, K. E. Lowry, M. M. Mills, and K. R. Arrigo (2013), Light and nutrient control of photosynthesis in natural phytoplankton populations from the Chukchi and Beaufort Seas, Arctic Ocean, *Limnol. Oceanogr.*, *58*, 2185–2205, doi:10.4319/lo.2013.58.6.2185.

Parkhill, K. L., and J. S. Gulliver (1999), Modeling the effect of light on whole-stream respiration, *Ecol. Model.*, *117*, 333–342.

Parkinson, C. L., and J. C. Comiso (2013), On the 2012 record low Arctic sea ice cover: Combined impact of preconditioning and an August storm, *Geophys. Res. Lett.*, *40*, 1356–1361, doi:10.1002/grl.50349.

Perovich, K., T. C. Grenfell, J. A. Richter-Menge, B. Light, W. B. Tucker, and H. Eicken (2003), Thin and thinner: Sea ice mass balance measurements during SHEBA, *J. Geophys. Res.*, *108*(C3), 8050, doi:10.1029/2001JC001079.

Perovich, D. K., B. Light, H. Eicken, K. F. Jones, K. Runciman, and S. V. Nghiem (2007), Increasing solar heating of the Arctic Ocean and adjacent seas, 1979-2005: Attribution and role in the ice-albedo feedback, *Geophys. Res. Lett.*, *34*, L19505, doi:10.1029/2007GL031480.

Platt, T., C. L. Gallegos, and W. G. Harrison (1980), Photoinhibition of photosynthesis in natural assemblages of marine phytoplankton, *J. Mar. Res.*, *38*, 687–701.

Robbins, L. L., J. G. Wynn, J. T. Lisle, K. K. Yates, P. O. Knorr, R. H. Byrne, X. Liu, M. C. Patsavas, K. Azetsu-Scott, and T. Takahashi (2013), Baseline monitoring of the western Arctic Ocean estimates 20% of Canadian Basin surface waters are undersaturated with respect to aragonite, *PLoS ONE*, *8*, e73796, doi:10.1371/journal.pone.0073796.

Rysgaard, S., R. N. Glud, M. K. Sejr, J. Bendtsen, and P. B. Christensen (2007), Inorganic carbon transport during sea ice growth and decay: A carbon pump in polar seas, *J. Geophys. Res.*, *112*, C03016, doi:10.1029/2006JC003572.

Sherr, B. F., and E. B. Sherr (2003), Community respiration/production and bacterial activity in the upper water column of the central Arctic Ocean, *Deep Sea Res., Part I*, *50*, 529–542.

Søreide, J. E., E. V. A. Leu, J. Berge, M. Graeve, and S. Falk-Petersen (2010), Timing of blooms, algal food quality and Calanus glacialis reproduction and growth in a changing Arctic, *Global Change Biol.*, *16*, 3154–3163.

Stanley, R. H. R., W. J. Jenkins, D. E. Lott, and S. C. Doney (2009), Noble gas constraints on air-sea gas exchange and bubble fluxes, *J. Geophys. Res.*, *114*, C11020, doi:10.1029/2009JC005396.

Steinacher, M., F. Joos, T. L. Frölicher, G.-K Plattner, and S. C. Doney (2009), Imminent ocean acidification in the Arctic projected with the NCAR global coupled carbon cycle-climate model, *Biogeosciences*, *6*, 515–533.

Timmermans, M.-L., J. Toole, A. Proshutinsky, R. Krishfield, and A. Plueddemann (2008), Eddies in the Canada Basin, Arctic Ocean, observed from ice-tethered profilers, *J. Phys. Oceanogr.*, *38*, 133–145.

Timmermans, M.-L., R. Krishfield, S. Laney, and J. Toole (2010), Ice-tethered profiler measurements of dissolved oxygen under permanent ice cover in the Arctic Ocean, *J. Atmos. Oceanic Technol.*, *27*, 1936–1949, doi:10.1175/2010JTECHO772.1.

Timmermans, M.-L., S. Cole, and J. Toole (2012), Horizontal density structure and restratification of the Arctic Ocean surface layer, *J. Phys. Oceanogr.*, *42*, 659–668, doi.org/10.1175/JPO-D-11-0125.1.

Toole, J. M., R. A. Krishfield, M.-L. Timmermans, and A. Proshutinsky (2011), The ice-tethered profiler: Argo of the Arctic, *Oceanography*, *24*, 126–135, doi:10.5670/oceanog.2011.64.

Toole, J. M., M.-L. Timmermans, D. K. Perovich, R. A. Krishfield, A. Proshutinsky, and J. A. Richter-Menge (2010), Influences of the ocean surface mixed layer and thermohaline stratification on Arctic Sea ice in the central Canada Basin, *J. Geophys. Res.*, *115*, C10018, doi:10.1029/2009JC005660.

Ulfsbo, A., N. Cassar, M. Korhonen, S. van Heuven, M. Hoppema, G. Kattner, and L. G. Anderson (2014), Late summer net community production in the central Arctic Ocean using multiple approaches, *Global Biogeochem. Cycles*, *28*, 1129–1148, doi:10.1002/2014GB004833.

van Heuven, S., D. Pierrot, J. W. B. Rae, E. Lewis, and D. W. R. Wallace (2011), *MATLAB Program Developed for CO_2 System Calculations*, *ORNL/CDIAC-105b*, Carbon Dioxide Inform. Anal. Cent., Oak Ridge Natl. Lab., U.S. Dep. of Energy, Oak Ridge, Tenn., doi:10.3334/CDIAC/otg.CO_2SYS_MATLAB_v1.1.

Wanninkhof, R. (2014), Relationship between wind speed and gas exchange over the ocean revisited, *Limnol. Oceanogr. Methods*, *12*(6), 351–362, doi:10.4319/lom.2014.12.351.

Yamamoto-Kawai, M., N. Tanaka, and S. Pivovarov (2005), Freshwater and brine behaviors in the Arctic Ocean deduced from historical data of $\delta^{18}O$ and alkalinity (1929-2002 A.D.), *J. Geophys. Res.*, *110*, C10003, doi:10.1029/2004JC 002793.

Yamamoto-Kawai, M., F. A. McLaughlin, E. C. Carmack, S. Nishino, K. Shimada and N. Kurita (2009a), Surface freshening of the Canada Basin, 2003–2007: River runoff versus sea ice meltwater, *J. Geophys. Res.*, *114*, C00A05, doi:10.1029/2008JC005000.

Yamamoto-Kawai, M., F. A. McLaughlin, E. C. Carmack, S. Nishino, and K. Shimada (2009b), Aragonite undersaturation in the Arctic Ocean: Effects of ocean acidification and sea ice melt, *Science*, *326*, 1098–1100, doi:10.1126/science. 1174190.

Yamamoto-Kawai, M., M., F. A. McLaughlin, and E. C. Carmack (2011), Effects of ocean acidification, warming and melting of sea ice on aragonite saturation of the Canada Basin surface water, *Geophys. Res. Lett.*, *38*, L03601, doi:10.1029/2010GL045501.

Zhang J., R. Lindsay, A. Schweiger, and M. Steel (2013), The impact of an intense summer cyclone on 2012 Arctic sea-ice retreat, *Geophys. Res. Lett.*, *40*, 720–726, doi:10.1002/grl.50190.